Dependence of the Thermal Conductivity of $BiFeO_3$ Thin Films on Polarization and Structure

Shuai Ning,[1,2] Samuel C. Huberman,[3] Chen Zhang,[1] Zhengjun Zhang,[2] Gang Chen,[3] and Caroline A. Ross[1,*]

[1]*Department of Materials Science and Engineering, Massachusetts Institute of Technology, Cambridge, Massachusetts 02139, USA*

[2]*Key Laboratory of Advanced Materials (MOE), School of Materials Science and Engineering, Tsinghua University, Beijing 100084, People's Republic of China*

[3]*Department of Mechanical Engineering, Massachusetts Institute of Technology, Cambridge, Massachusetts 02139, USA*

(Received 19 June 2017; published 29 November 2017)

The role of the ferroelectric polarization state and crystal structure in determining the room-temperature thermal conductivity of epitaxial $BiFeO_3$ thin films is investigated. The ferroelectric domain configuration is varied by changing the oxygen partial pressure during growth, as well as by polarizing the samples by the application of an *in situ* electric field during the thermal conductivity measurement. However, little or no dependence of thermal conductivity on the ferroelectric domain structure is observed. In contrast, the thermal conductivity significantly depends on the morphotropic phase structure, being about 2/3 as large in tetragonal-like compared to rhombohedral-like $BiFeO_3$ film. The substantial structural dependence of thermal conductivity found here may provide a route to reversible manipulation of thermal properties.

DOI: 10.1103/PhysRevApplied.8.054049

I. INTRODUCTION

Manipulating the thermal properties and controlling the flow of heat in solid-state materials is of great importance for many technologies including thermal management, energy harvesting, and sensing [1]. Though there are numerous reports on the manipulation of phonon transport at room temperature through physical phase transformations [2–5], chemical composition modification [6], and defect engineering [7–9], challenges remain in reversibly tuning the thermal conductivity in a material. Recently, domain walls in ferroelectric materials, which represent coherent boundaries with a thickness of a few nanometers, have been reported in a handful of studies to have an effect on the thermal conductivity [10–12], potentially providing a method to reversibly manipulate the thermal conductivity. However, the role that ferroelectric domain walls play in tuning phonon transport is incompletely understood, and the effect of other factors including grain boundaries and other defects in polycrystalline ferroelectric materials [10] and the substrate surface [11] complicate the analysis. Even if domain walls play a significant role, the reported magnitude of the thermal conductivity change caused by manipulating ferroelectric domains appears quite small in terms of practical applications. It is, therefore, of great interest to investigate the factors that affect the thermal conductivity of ferroelectric materials.

$BiFeO_3$ (BFO), a lead-free single-phase ferroelectric material, has attracted much attention owing to its interesting physical properties including multiferroicity [13]. Bulk BFO exhibits a rhombohedral structure in which oxygen octahedra are slightly tilted from the center of symmetry along the $\langle 111 \rangle$ pseudocubic direction. When epitaxially grown on perovskite substrates such as $SrTiO_3$ (STO), a small monoclinic distortion of the rhombohedral structure is present, and the structure is denoted as *R*-like BFO. In general, *R*-like BFO tends to polarize along the $\langle 111 \rangle$ directions [14], resulting in eight possible domain variants with both in-plane and out-of-plane components, which is undesirable for practical applications. As a result, domain engineering of BFO thin films has been widely explored to improve the ferroelectric performance, such as by utilizing vicinal substrates [15,16] and tuning the buffer thickness [16,17]. Recently, an approach for domain engineering of BFO thin films has emerged with the observation of a new polymorph with a large c/a ratio (approximately 1.25) stabilized by much larger in-plane compressive strain (>4.5%) [18], which is tetragonal with a slight monoclinic distortion [19] and denoted as *T*-like BFO. This new polymorph is predicted to show many fascinating properties, such as a simpler switching process and higher remnant polarization. In particular, a reversible morphotropic phase transformation between *R*- and *T*-like BFO can be driven by simple stimuli [20–22], and the morphotropic phase boundary shows a strong electromechanical response [23,24].

In this paper, we investigate the thermal transport properties of epitaxial *R*- and *T*-like BFO thin films and the dependence of thermal conductivity on the polarization state. The two polymorphs are obtained by substrate strain engineering, and the film strain state as well as the ferroelectric domain features are controlled via the oxygen partial pressure during deposition. The room-temperature thermal conductivity is found to be almost independent of the oxygen

*Corresponding author.
caross@mit.edu

partial pressure. Through piezoresponse-force-microscopy (PFM) characterization and thermal analysis with an *in situ* electric field, we find the domain-wall density does not play a significant role in determining the thermal conductivity, whereas the thermal conductivity is approximately $2/3$ as great for the T-like BFO than for the R-like BFO.

II. EXPERIMENT

BFO thin films of (28–38)-nm thickness are prepared by pulsed-laser deposition (PLD) using a KrF excimer laser ($\lambda = 248$ nm) with 15-J/cm^2 fluence and 10-Hz pulse repetition rate, at a substrate temperature of 650 °C and under different oxygen pressures, i.e., 5, 50, and 100 mTorr. A Bi-rich $Bi_{1.2}FeO_3$ target is used to compensate for Bi loss during deposition, and (001)-oriented STO (or with 0.7-wt % Nb doping) and $LaAlO_3$ (LAO) are used as substrates. Additionally, BFO films are grown on an approximately 17-nm $La_{0.66}Sr_{0.33}MnO_3$ (LSMO) epitaxial layer that is first prepared by PLD at 800 °C under an oxygen pressure of 10 mTorr on LAO, as well as on an approximately 22-nm $SrRuO_3$ (SRO) layer grown at 850 °C under an oxygen pressure of 5 mTorr on LAO. The film or layer thickness is determined by x-ray reflectometry (XRR). Structural characterization is carried out by high-resolution x-ray diffraction (HRXRD) and reciprocal-space mapping (RSM) on a Bruker D8 Discover x-ray diffractometer. The chemical composition and defect properties are examined by x-ray photoelectron spectroscopy (XPS, ESCALAB 250Xi). The Raman spectra are measured at room temperature using a Horiba LabRAM 800 HR spectrometer equipped with a He-Ne (632.8-nm) laser as the excitation source.

The ferroelectric domain structures are characterized using PFM on a Veeco Nanoscope V atomic force microscope operated in tapping mode and near the contact resonance of the tip-sample configuration for a better signal-to-noise ratio. A Precision Premier II Ferroelectric Tester is utilized to measure the polarization-electric (P-E) field loops at a frequency of 1 kHz with voltages of a few volts. The room-temperature thermal conductivity is analyzed by a homemade time-domain thermoreflectance (TDTR) setup with Al layers as the transducer pads on the top of the sample surface, which is sensitive to the thermal conductivity across the film plane, perpendicular to the sample surface. The *in situ* TDTR measurements are conducted with a layer of Au(100 nm)/Ta(5 nm) as the transducer pads, which are prepared by sputtering with a diameter of 150 μm. The Precision Premier II Ferroelectric Tester is used to apply the dc bias for the *in situ* TDTR measurements via a probe station contacting the Au/Ta pads.

III. RESULTS AND DISSCUSSION

Structural characterizations by HRXRD are summarized in Fig. 1. No secondary-phase peaks can be seen, indicating that single-phase BFO is obtained in each case. Comparing the XRD results of BFO films grown at 5 mTorr on different substrates, one may see that the crystalline structure can be effectively manipulated by substrate strain engineering. Specifically, the approximately 30-nm BFO film grown on STO, as well as on SRO/LAO, exhibits a typical R-like structure, while that grown on LAO and LSMO/LAO has a qualitatively different diffraction pattern corresponding to T-like BFO. A slight shift of the BFO diffraction peak shown in both Figs. 1(a) and 1(b) suggests the BFO films grown on bare substrates and on a bottom layer are under different strain states.

Reciprocal-space mapping is collected in the same instrument using the asymmetric (103) or (113) family of peaks. The split of the (103) signals of the T-like BFO shown in Fig. S1 of Ref. [25] clearly indicates a slight monoclinic distortion along the $\langle 100 \rangle$ direction [23]. The structural information interpreted from RSM analysis (see Table I) demonstrates a significant structural difference between the two polymorphs seen in the much larger c/a ratio and unit-cell volume in T-like BFO compared to R-like BFO, as illustrated by the ideal crystalline structure shown in the inset of Figs. 1(a) and 1(b). Meanwhile, the R-like BFO grown on SRO/LAO shows more relaxation in comparison with that on STO, due to the larger in-plane lattice parameters of the SRO layer on LAO compared to the STO bare substrate. For T-like BFO, there is little difference between the film peak positions for the samples on LSMO/LAO and on LAO as a consequence of the similar in-plane lattice parameters of the LSMO layer and the LAO bare substrate.

Additionally, T-like BFO films are grown on LAO, and R-like films are grown on STO under oxygen pressures of 5, 50, and 100 mTorr. Adjusting the oxygen partial pressure during deposition does not change the crystalline structure, but it impacts the strain state suggested by the clear shift of the diffraction peaks shown in Figs. 1(c) and 1(d). The detailed structural information shown in Table I, as well as Fig. S1 of Ref. [25], clearly shows that higher oxygen pressure leads to a smaller out-of-plane lattice parameter and a larger in-plane lattice parameter but little change in the unit-cell volume, and more relaxation occurs when grown under higher oxygen pressure.

The room-temperature thermal conductivity is analyzed by TDTR methods as described elsewhere [26–28], and further details are given in Ref. [25]. The thermal conductivities of the underlying layers (LSMO and SRO) and the bare substrates (STO and LAO) are first analyzed and then used as known with other input parameters [29–33] in the nonlinear least-squares minimization fitting procedure to obtain the cross-plane thermal conductivity of BFO thin films. Figure 2 shows the room-temperature thermal conductivity of four pairs of BFO samples. Each pair is from the same deposition run and has the same film thickness. Comparing the results of BFO/STO and BFO/SRO/LAO grown under the same oxygen pressure, as well

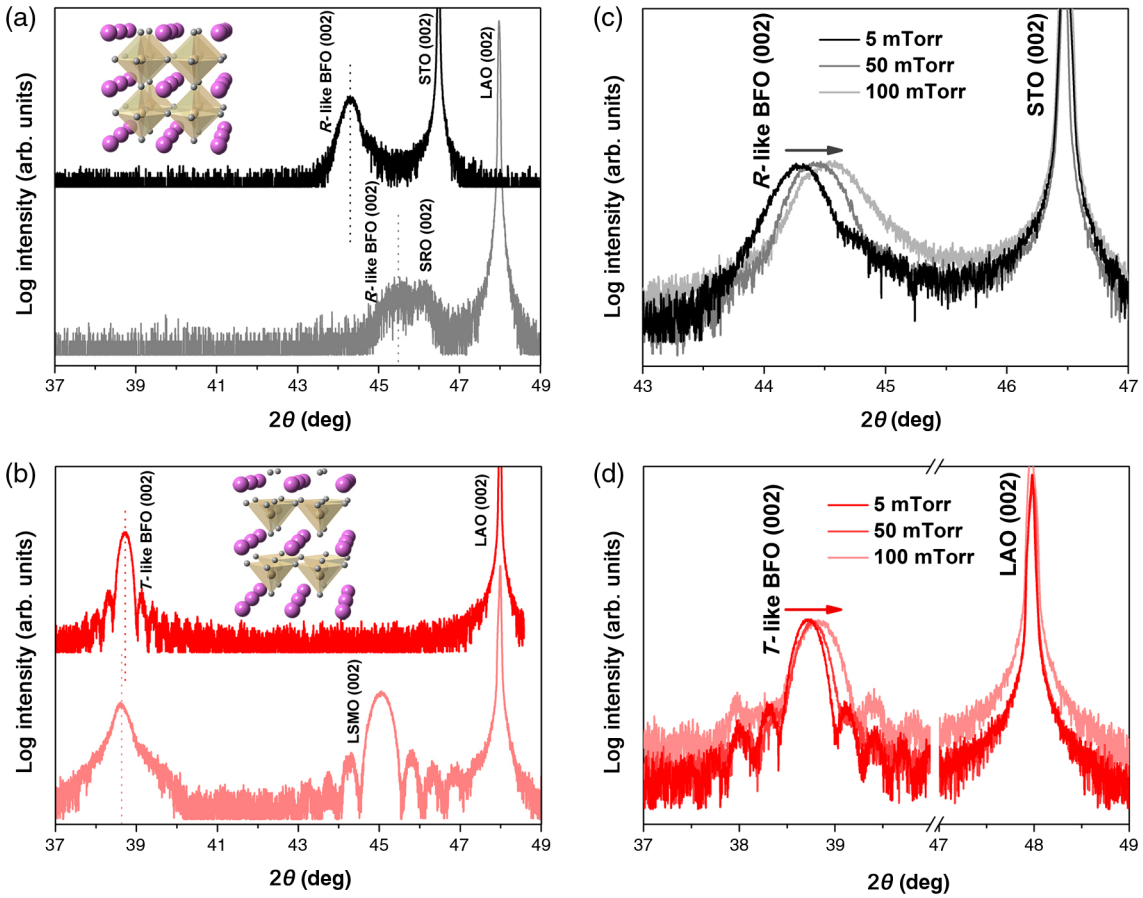

FIG. 1. HRXRD structural characterizations: (a) *R*-like BFO films grown on STO and SRO/LAO at 5-mTorr oxygen, (b) *T*-like BFO films grown on LAO and LSMO/LAO at 5-mTorr oxygen, (c) *R*-like BFO films on STO, and (d) *T*-like BFO films on LAO grown under different oxygen partial pressures of 5, 50, and 100 mTorr. The ideal crystalline structure of rhombohedral BFO and tetragonal BFO is shown in the insets of (a) and (b), respectively.

as BFO/LAO and BFO/LSMO/LAO, one can observe that the thermal conductivity is independent of the underlayers or substrates, indicating that the fitting procedure of the TDTR data analysis is reasonable. In addition, two interesting phenomena can be seen. First, the thermal conductivity is almost independent of the oxygen pressure for each polymorph despite the varying film strain states. Second, the thermal conductivity is significantly dependent on the crystal structure, with the consistent value of *T*-like BFO approximately 2/3 that of *R*-like BFO.

TABLE I. The structural characterization results of BFO films on different substrates.

Sample	BFO phase	Substrate lattice parameter (Å)	BFO film lattice parameter (Å)	Unit-cell volume (Å^3)	c/a ratio
BFO/STO 5 mTorr	*R*-like	$a_{STO} = c_{STO} = 3.905$	$a = 3.900$ $c = 4.093$	62.25	1.049
BFO/STO 100 mTorr	*R*-like	$a_{STO} = c_{STO} = 3.905$	$a = 3.904$ $c = 4.067$	61.98	1.042
BFO/SRO/LAO 5 mTorr	*R*-like	$a_{SRO} = 3.947\, c_{SRO} = 3.930$	$a = 3.942$ $c = 3.930$	61.07	0.997
BFO/STO 5 mTorr	*T*-like	$a_{LAO} = c_{LAO} = 3.788$	$a = 3.778$ $c = 4.689$	66.93	1.241
BFO/STO 100 mTorr	*T*-like	$a_{LAO} = c_{LAO} = 3.788$	$a = 3.783$ $c = 4.621$	66.13	1.222
BFO/SRO/LAO 5 mTorr	*T*-like	$a_{LSMO} = 3.776\, c_{LSMO} = 4.007$	$a = 3.772$ $c = 4.710$	67.10	1.249

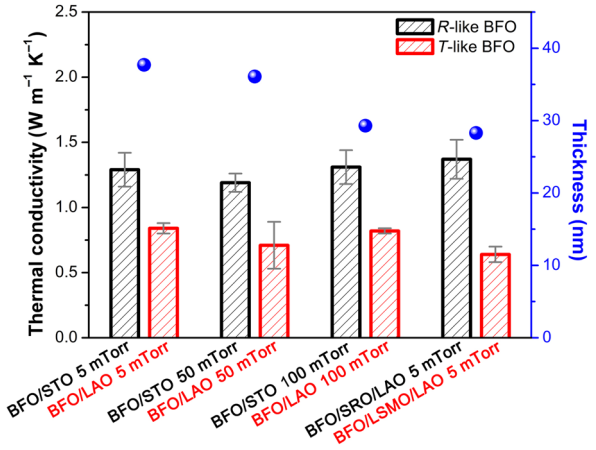

FIG. 2. Room-temperature thermal conductivity analyzed by TDTR and BFO thickness by XRR of both *R*- and *T*-like BFO films prepared on different substrates and under different oxygen partial pressures.

The chemical composition and defect properties are examined by high-resolution XPS on three representative samples, i.e., *T*-like BFO/LAO grown at 5 mTorr and *R*-like BFO/STO grown at 5 and 100 mTorr, denoted as *T*-5, *R*-5, and *R*-100, respectively. Before measurements, all samples are sputtered by Ar^+ for 5 min to remove surface contamination. From the XPS of Bi shown in Fig. 3(a), one can see all samples exhibit two pairs of 4*f* peaks: the one with higher binding energy corresponds to Bi^{3+}, and the other one with lower binding energy corresponds to Bi with a lower valence state, probably created by the Ar^+ sputtering. The Fe 2*p* core-level spectra can be fitted by one pair of peaks shown in Fig. 3(c). Together with the satellite features of Fe 2*p*, we conclude that the Fe ions are in a +3 valence state. Additionally, the well-fitted symmetric peaks of the O 1*s* core level shown in Fig. 3(b) indicate the amount of oxygen vacancies is quite low. The peak position and relative intensity of Bi, O, and Fe seem very similar in *R*-5 and *R*-100, which means the defect states of the samples do not differ greatly with the oxygen partial pressure during PLD.

The ferroelectric domain features are examined by PFM, which is sensitive to the out-of-plane component of the polarization, on four representative samples, i.e., *T*-like BFO/LSMO/LAO grown at 5 and 100 mTorr and *R*-like BFO/Nb:STO grown at 5 and 100 mTorr, denoted as *T*-5, *T*-100, *R*-5, and *R*-100, respectively. The *R*-like BFO/Nb:STO is used for PFM characterization instead of *R*-like BFO/SRO/LAO because the surface of the latter has higher roughness. There is no difference in the BFO peak position between the films on STO and on Nb:STO (see Fig. S3 in Ref. [25]).

Figure 4 shows the PFM phase images, where contrast can be clearly seen in all the samples, indicating ferroelectric domains with different out-of-plane components coexist in each as-grown sample. A stripelike domain structure can be seen in both *T*-like samples, while a qualitatively different mosaiclike domain pattern exists in the *R*-like samples. The domain size, shape, and density vary considerably with the oxygen pressure during deposition, suggesting that adjusting the oxygen pressure during deposition can be an approach to domain engineering in both *R*- and *T*-like polymorphs [34]. This phenomenon may be a result of changes in the surface chemistry during growth at different oxygen pressures in order to achieve charge compensation and maintain the polarization [35,36] or a consequence of structural relaxation. The micrometers-long stripes in *T*-100 shown in Fig. 4(b) appear to be much narrower than those in *T*-5 [see Fig. 4(a)], leading to a much higher domain-wall density. Meanwhile, both of them exhibit a weak vertical PFM contrast, indicating those

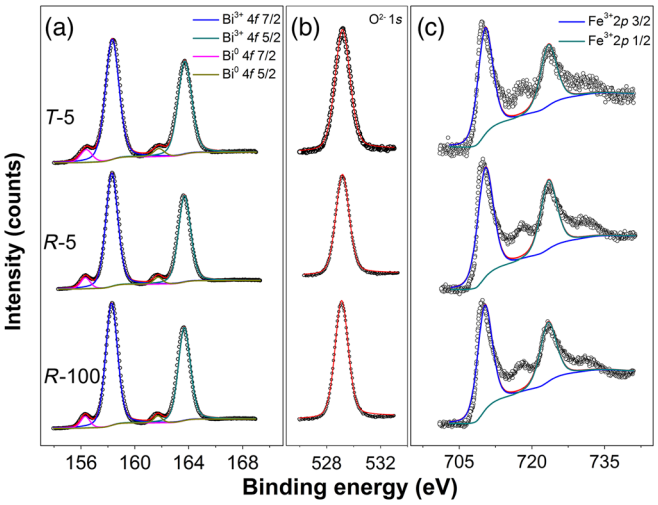

FIG. 3. High-resolution XPS analysis of (a) Bi, (b) O, and (c) Fe in samples *T*-5, *R*-5, and *R*-100.

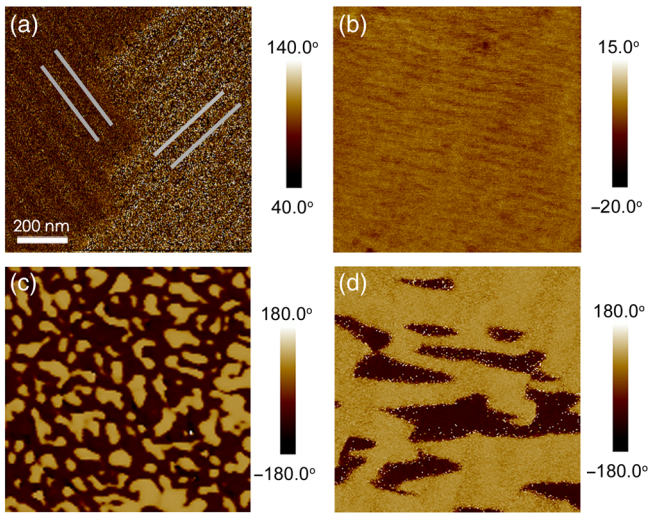

FIG. 4. Vertical PFM phase images of (a) *T*-5, (b) *T*-100, (c) *R*-5, and (d) *R*-100.

domains might have an in-plane polarization component due to a deviation of the ferroelectric axis from the *c* axis [37]. As for the *R*-like samples, the domains of *R*-5 are more random, much smaller, and of a higher density than *R*-100. As suggested by previous work [38], the phase image of *R*-5 in Fig. 4(c) indicates eight possible domain variants might coexist, resulting in three possible polarization angles at the domain walls (180°, 71°, and 109° boundaries, where the latter two are ferroelastic), which can be charged or neutral. In comparison, the image of *R*-100 in Fig. 4(d) is characteristic of a system with fewer possible domain variants [11] and lower domain-wall density. The slightly lower thermal conductivity of *R*-5 ($1.29\ \mathrm{W\,m^{-1}\,K^{-1}}$) compared to *R*-100 ($1.32\ \mathrm{W\,m^{-1}\,K^{-1}}$), as well as the lower thermal conductivity of *T*-100 ($0.82\ \mathrm{W\,m^{-1}\,K^{-1}}$) compared to *T*-5 ($0.84\ \mathrm{W\,m^{-1}\,K^{-1}}$), could be a consequence of the contribution of domain walls to phonon scattering, although this effect seems to be negligible.

The ferroelectric hysteresis of both *R*-5 and *T*-5 is measured using the PFM. Typical out-of-plane *P*-*E* loops are obtained in both cases shown in Figs. 5(a) and 5(b). The larger coercivity and weaker piezoresponse suggest a more complicated polarization-switching mechanism in the *R*-like BFO samples. A dc bias of $+6\ \mathrm{V}/-6\ \mathrm{V}$, which seems sufficient to polarize both BFO polymorph films based on the hysteresis loops, is used to conduct the writing and rewriting switching experiments. The respective phase images are immediately collected after removing the bias. The clear phase contrast shown in Figs. 5(c) and 5(d) indicates both *R*- and *T*-like BFO samples can be polarized and switched at a bias of approximately 6 V and that the domain-wall density can be significantly tuned by the external electric field.

To further investigate the role that domain walls play in determining the thermal conductivity, *in situ* TDTR measurements, in which the thermal analysis is performed

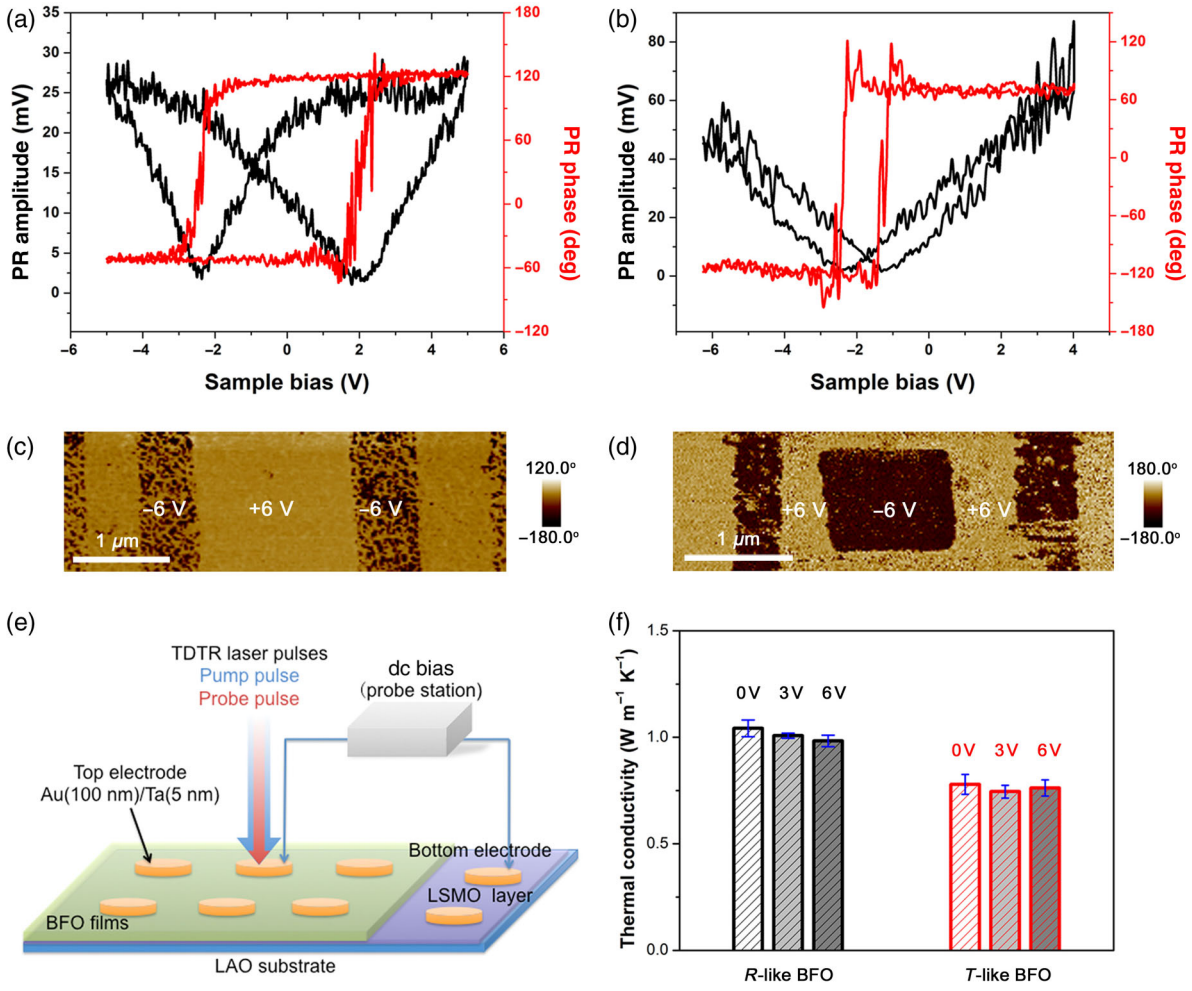

FIG. 5. *In situ* TDTR analysis: Local PE amplitude and phase data measured by PFM of (a) *R*-like BFO(30 nm)/Nb:STO and (b) *T*-like BFO(30 nm)/LSMO(17 nm)/LAO grown under an oxygen pressure of 5 mTorr. The writing and rewriting switching PFM phase images of (c) *R*-like and (d) *T*-like BFO. (e) The schematic of *in situ* TDTR measurements. (f) The thermal conductivity of both *R*- and *T*-like BFO samples from *in situ* TDTR measurements.

simultaneously with changing the domain configuration, are valuable. The layout of the PFM instrument precludes access by the TDTR laser, so instead, the *in situ* measurements are done by applying the dc bias through top electrodes during the TDTR measurement, as shown schematically in Fig. 5(e). Out-of-plane *P*-*E* loops are first measured within the *in situ* TDTR setup (see Fig. S4 in Ref. [25]) showing that both *R*- and *T*-like samples can be polarized by a dc bias; i.e., the domain-wall density will change significantly during application of a voltage. The domain wall can be in three different configurations. Walls such as Fig. 6(c), orthogonal to the heat flow, are expected to affect heat flow analogous to the interfaces of a multilayered film affecting cross-plane thermal conductivity. However, given the small film thickness, we expect most domain walls to be oriented through the film thickness which is parallel or at an angle to the direction of heat flow in the TDTR measurements as in Figs. 6(a) and 6(b), respectively.

In situ TDTR data are collected on both *T*-5 and *R*-5 samples (see Fig. S5 in Ref. [25]). The results shown in Fig. 5(f) suggest the conductivity of the *R*-like BFO film is slightly reduced or unchanged with an applied bias, while that of the *T*-like BFO does not show a clear decrease considering the limits in accuracy of the measurement. For *T*-like (001) epitaxial BFO films, which are predicted to be polarized out of plane, it is possible that the insensitivity of thermal conductivity to domain-wall density in the *in situ* experiment occurs because polarization changes are accomplished by movement of only 180° walls which are not ferroelastic and will not be expected to interact strongly with phonons due to no structural distortion. As for *R*-like (001) BFO epitaxial films, however, prior work has shown that an out-of-plane voltage can result in not only 180° switching but also 71° and 109°. The phase-field simulation suggests that the activation energy for direct 180° switching is higher than that for 71°, leading to a relaxation-mediated 180° switching path for *R*-like BFO in which the out-of-plane electric field induced 71° switching, and the unstable 71° domains then relax into the stable 180° ones at remanence [39]. Further experimental study indicates a phase-dependent switching mechanism in *R*-like BFO in which ferroelastic polarization rotations (71° or 109°) become dominant as the applied bias increases, instead of ferroelectric switching (180°), whereas switching using a top electrode leads only to ferroelastic switching, which is because electrodes with larger area can stabilize 71° domains due to larger domain size [39–41]. The 150-μm top electrodes we use in the *in situ* TDTR measurement can plausibly involve substantial ferroelastic domain walls, which can contribute to increased phonon scattering and the reduction of thermal conductivity. However, the observed decrease of thermal conductivity is quite small, indicating that the domain-wall density has a relatively minor influence on the thermal conductivity.

As to the significant dependence of thermal conductivity on the polymorph, it may originate from the differences in structure and ionic coordination. Raman measurements are carried out at room temperature. From the results shown in Figs. 7(a) and 7(b), five Raman peaks from the BFO/STO sample can be identified as typical phonon modes of *R*-like BFO with $R3c$ symmetry, while seven peaks from the BFO/LAO sample can be clearly ascribed to *T*-like BFO with Cc symmetry [42,43]. The peaks in the *R*-like BFO film are superposed on a strong fluorescence signal from the STO substrate, but weak peaks are evident, as seen in the thin BFO films of Ref. [44]. Given that there are more atoms in the T-like BFO unit cell than in the B-like BFO unit cell, there are consequently more phonon branches [42] available to satisfy the scattering selection rules to yield a reduced thermal conductivity in T-like BFO when compared to B-like BFO. In addition, the distortion of oxygen octahedra caused by the larger c/a ratio may lead to a much weaker Fe—O bonding along the $\langle 001 \rangle$ direction in *T*-like BFO. The reduced thermal conductivity of *T*-like BFO can be also understood as a result of this weaker interlayer coupling and increased anharmonicity for *T*-like BFO.

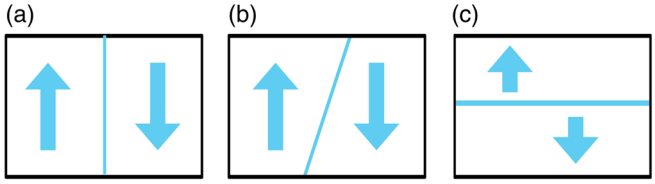

FIG. 6. Possible domain-wall configurations: (a) normal, (b) oblique, and (c) parallel to the surface of sample.

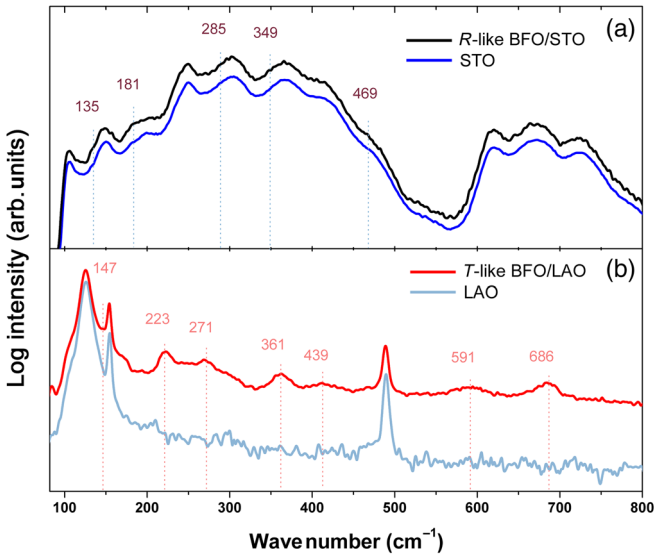

FIG. 7. Raman spectra of (a) *R*-like and (b) *T*-like BFO thin films and bare substrates.

IV. CONCLUSION

Two different polymorphs of PLD-grown epitaxial BFO thin films, i.e., *R*-like and *T*-like BFO, are obtained by substrate strain engineering. The as-grown ferroelectric domain features of each polymorph are quite different: *T*-like BFO shows a periodic stripelike domain pattern, while *R*-like shows a mosaic domain structure. The oxygen pressure has a substantial effect on the ferroelectric domain morphology for each polymorph, providing a convenient method for domain engineering. However, the oxygen partial pressure during deposition has only modest influence on the film strain and defect levels, which are predicted to influence the thermal conductivity [45,46].

There is little difference in thermal conductivity with oxygen pressure, suggesting that the domain configuration for either *R*-like or *T*-like samples does not greatly influence the thermal conductivity. Further *in situ* TDTR analysis, in which the domain state is changed by applying a voltage during the thermal conductivity measurement, also supports the conclusion that domain-wall density in the films and geometry studied here has only minor effects on the thermal transport. However, a substantial dependence of thermal conductivity on the morphotropic phase structure is observed. The thermal conductivity of *T*-like BFO is about 2/3 that of *R*-like BFO. In comparison with the effects of domain walls in our work, as well as that reported in Ref. [11], the structural dependence of thermal conductivity observed here has a much greater effect, suggesting that the morphotropic phase transformation can be used to control the thermal properties of BFO thin films.

ACKNOWLEDGMENTS

This work is sponsored by the Solid-State Solar-Thermal Energy Conversion Center under Grant No. DE-SC0001299/DE-FG02-09ER46577. Shared facilities of the MIT MRSEC through the MRSEC Program of the National Science Foundation under Grant No. DMR-1419807 are used.

[1] E. S. Toberer, L. L. Baranowski, and C. Dames, Advances in thermal conductivity, Annu. Rev. Mater. Res. **42**, 179 (2012).

[2] D.-W. Oh, C. Ko, S. Ramanathan, and D. G. Cahill, Thermal conductivity and dynamic heat capacity across the metal-insulator transition in thin film VO_2, Appl. Phys. Lett. **96**, 151906 (2010).

[3] R. Zheng, J. Gao, J. Wang, and G. Chen, Reversible temperature regulation of electrical and thermal conductivity using liquid-solid phase transitions, Nat. Commun. **2**, 289 (2011).

[4] H. Ji, D. P. Sellan, M. T. Pettes, X. Kong, J. Ji, L. Shi, and R. S. Ruoff, Enhanced thermal conductivity of phase change materials with ultrathin-graphite foams for thermal energy storage, Energy Environ. Sci. **7**, 1185 (2014).

[5] Z. Guo, S. J. Yoon, J. S. Manser, P. V. Kamat, and T. Luo, Structural phase-and degradation-dependent thermal conductivity of $CH_3NH_3PbI_3$ perovskite thin films, J. Phys. Chem. C **120**, 6394 (2016).

[6] J. Cho, M. D. Losego, H. G. Zhang, H. Kim, J. Zuo, I. Petrov, D. G. Cahill, and P. V. Braun, Electrochemically tunable thermal conductivity of lithium cobalt oxide, Nat. Commun. **5**, 4035 (2014).

[7] S. Dhara, H. S. Solanki, V. Singh, S. Sengupta, B. Chalke, A. Dhar, M. Gokhale, A. Bhattacharya, and M. M. Deshmukh, Tunable thermal conductivity in defect engineered nanowires at low temperatures, Phys. Rev. B **84**, 121307 (2011).

[8] K. E. Meyer, R. Cheaito, E. Paisley, C. T. Shelton, J. L. Braun, J.-P. Maria, J. F. Ihlefeld, and P. E. Hopkins, Crystalline coherence length effects on the thermal conductivity of MgO thin films, J. Mater. Sci. **51**, 10408 (2016).

[9] B. F. Donovan, E. Sachet, J.-P. Maria, and P. E. Hopkins, Interplay between mass-impurity and vacancy phonon scattering effects on the thermal conductivity of doped cadmium oxide, Appl. Phys. Lett. **108**, 021901 (2016).

[10] J. F. Ihlefeld, B. M. Foley, D. A. Scrymgeour, J. R. Michael, B. B. McKenzie, D. L. Medlin, M. Wallace, S. Trolier-McKinstry, and P. E. Hopkins, Room-temperature voltage tunable phonon thermal conductivity via reconfigurable interfaces in ferroelectric thin films, Nano Lett. **15**, 1791 (2015).

[11] P. E. Hopkins, C. Adamo, L. Ye, B. D. Huey, S. R. Lee, D. G. Schlom, and J. F. Ihlefeld, Effects of coherent ferroelastic domain walls on the thermal conductivity and Kapitza conductance in bismuth ferrite, Appl. Phys. Lett. **102**, 121903 (2013).

[12] J.-J. Wang, Y. Wang, J. F. Ihlefeld, P. E. Hopkins, and L.-Q. Chen, Tunable thermal conductivity via domain structure engineering in ferroelectric thin films: A phase-field simulation, Acta Mater. **111**, 220 (2016).

[13] T. Zhao, A. Scholl, F. Zavaliche, K. Lee, M. Barry, A. Doran, M. Cruz, Y. Chu, C. Ederer, and N. Spaldin, Electrical control of antiferromagnetic domains in multiferroic $BiFeO_3$ films at room temperature, Nat. Mater. **5**, 823 (2006).

[14] G. Catalan and J. F. Scott, Physics and applications of bismuth ferrite, Adv. Mater. **21**, 2463 (2009).

[15] Y. H. Chu, M. P. Cruz, C. H. Yang, L. W. Martin, P. L. Yang, J. X. Zhang, K. Lee, P. Yu, L. Q. Chen, and R. Ramesh, Domain control in multiferroic $BiFeO_3$ through substrate vicinality, Adv. Mater. **19**, 2662 (2007).

[16] Y.-H. Chu, Q. He, C.-H. Yang, P. Yu, L. W. Martin, P. Shafer, and R. Ramesh, Nanoscale control of domain architectures in $BiFeO_3$ thin films, Nano Lett. **9**, 1726 (2009).

[17] M. Trassin, G. D. Luca, S. Manz, and M. Fiebig, Probing ferroelectric domain engineering in $BiFeO_3$ thin films by second harmonic generation, Adv. Mater. **27**, 4871 (2015).

[18] R. Zeches, M. Rossell, J. Zhang, A. Hatt, Q. He, C.-H. Yang, A. Kumar, C. Wang, A. Melville, and C. Adamo, A strain-driven morphotropic phase boundary in $BiFeO_3$, Science **326**, 977 (2009).

[19] H. M. Christen, J. H. Nam, H. S. Kim, A. J. Hatt, and N. A. Spaldin, Stress-induced R-M_A-M_C-T symmetry changes in $BiFeO_3$ films, Phys. Rev. B **83**, 144107 (2011).

[20] D. Mazumdar, V. Shelke, M. Iliev, S. Jesse, A. Kumar, S. V. Kalinin, A. P. Baddorf, and A. Gupta, Nanoscale switching

characteristics of nearly tetragonal $BiFeO_3$ thin films, Nano Lett. **10**, 2555 (2010).

[21] C. Beekman, W. Siemons, T. Z. Ward, M. Chi, J. Howe, M. D. Biegalski, N. Balke, P. Maksymovych, A. Farrar, and J. Romero, Phase transitions, phase coexistence, and piezoelectric switching behavior in highly strained $BiFeO_3$ films, Adv. Mater. **25**, 5561 (2013).

[22] C.-H. Chiu, W.-I. Liang, C.-W. Huang, J.-Y. Chen, Y.-Y. Liu, J.-Y. Li, C.-L. Hsin, Y.-H. Chu, and W.-W. Wu, Atomic visualization of the phase transition in highly strained $BiFeO_3$ thin films with excellent pyroelectric response, Nano Energy **17**, 72 (2015).

[23] A. J. Hatt, N. A. Spaldin, and C. Ederer, Strain-induced isosymmetric phase transition in $BiFeO_3$, Phys. Rev. B **81**, 054109 (2010).

[24] J. Zhang, Q. He, M. Trassin, W. Luo, D. Yi, M. Rossell, P. Yu, L. You, C. Wang, and C. Kuo, Microscopic Origin of the Giant Ferroelectric Polarization in Tetragonal-Like $BiFeO_3$, Phys. Rev. Lett. **107**, 147602 (2011).

[25] See Supplemental Material at http://link.aps.org/supplemental/10.1103/PhysRevApplied.8.054049 for RSM analysis, TDTR methods, *P-E* loops, and raw data for *in situ* TDTR measurements.

[26] W. S. Capinski and H. J. Maris, Improved apparatus for picosecond pump-and-probe optical measurements, Rev. Sci. Instrum. **67**, 2720 (1996).

[27] D. G. Cahill, K. Goodson, and A. Majumdar, Thermometry and thermal transport in micro/nanoscale solid-state devices and structures, J. Heat Transfer **124**, 223 (2002).

[28] A. J. Schmidt, X. Chen, and G. Chen, Pulse accumulation, radial heat conduction, and anisotropic thermal conductivity in pump-probe transient thermoreflectance, Rev. Sci. Instrum. **79**, 114902 (2008).

[29] J. Chen, W. Wang, J.-B. Li, and G. Rao, X-ray diffraction analysis and specific heat capacity of $(Bi_{1-x}La_x)FeO_3$ perovskites, J. Alloys Compd. **459**, 66 (2008).

[30] L.-M. Wang, J.-H. Lai, J.-I. Wu, Y.-K. Kuo, and C. Chang, Effects of Ru substitution for Mn on $La_{0.7}Sr_{0.3}MnO_3$ perovskites, J. Appl. Phys. **102**, 023915 (2007).

[31] F. Castelpoggi, L. Morelli, H. Salva, S. Cuffini, R. Carbonio, and R. Sanchez, Specific heat measurement of the magnetoresistant perovskite $SrRuO_3$, Solid State Commun. **101**, 597 (1997).

[32] A. Durán, F. Morales, L. Fuentes, and J. Siqueiros, Specific heat anomalies at 37, 105 and 455 K in $SrTiO_3$: Pr, J. Phys. Condens. Matter **20**, 085219 (2008).

[33] W. Schnelle, R. Fischer, and E. Gmelin, Specific heat capacity and thermal conductivity of $NdGaO_3$ and $LaAlO_3$ single crystals at low temperatures, J. Phys. D **34**, 846 (2001).

[34] M. Highland, T. Fister, D. Fong, P. Fuoss, C. Thompson, J. Eastman, S. Streiffer, and G. Stephenson, Equilibrium Polarization of Ultrathin $PbTiO_3$ with Surface Compensation Controlled by Oxygen Partial Pressure, Phys. Rev. Lett. **107**, 187602 (2011).

[35] R. V. Wang, D. D. Fong, F. Jiang, M. J. Highland, P. H. Fuoss, C. Thompson, A. M. Kolpak, J. A. Eastman, S. K. Streiffer, A. M. Rappe, and G. B. Stephenson, Reversible Chemical Switching of a Ferroelectric Film, Phys. Rev. Lett. **102**, 047601 (2009).

[36] M. J. Highland, T. T. Fister, M. I. Richard, D. D. Fong, P. H. Fuoss, C. Thompson, J. A. Eastman, S. K. Streiffer, and G. B. Stephenson, Polarization Switching without Domain Formation at the Intrinsic Coercive Field in Ultrathin Ferroelectric $PbTiO_3$, Phys. Rev. Lett. **105**, 167601 (2010).

[37] H.-J. Liu, Y.-H. Du, P. Gao, Y.-C. Huang, H.-W. Chen, Y.-C. Chen, H.-L. Liu, Q. He, Y. Ikuhara, and Y.-H. Chu, Tetragonal $BiFeO_3$ on yttria-stabilized zirconia, APL Mater. **3**, 116104 (2015).

[38] J. Desmarais, J. F. Ihlefeld, T. Heeg, J. Schubert, D. G. Schlom, and B. D. Huey, Mapping and statistics of ferroelectric domain boundary angles and types, Appl. Phys. Lett. **99**, 162902 (2011).

[39] S. Baek, H. Jang, C. Folkman, Y. Li, B. Winchester, J. Zhang, Q. He, Y. Chu, C. Nelson, and M. Rzchowski, Ferroelastic switching for nanoscale non-volatile magnetoelectric devices, Nat. Mater. **9**, 309 (2010).

[40] F. Zavaliche, P. Shafer, R. Ramesh, M. Cruz, R. Das, D. Kim, and C. Eom, Polarization switching in epitaxial $BiFeO_3$ films, Appl. Phys. Lett. **87**, 252902 (2005).

[41] M. Cruz, Y. Chu, J. Zhang, P. Yang, F. Zavaliche, Q. He, P. Shafer, L. Chen, and R. Ramesh, Strain Control of Domain-Wall Stability in Epitaxial $BiFeO_3$ (110) Films, Phys. Rev. Lett. **99**, 217601 (2007).

[42] M. Iliev, M. Abrashev, D. Mazumdar, V. Shelke, and A. Gupta, Polarized Raman spectroscopy of nearly tetragonal $BiFeO_3$ thin films, Phys. Rev. B **82**, 014107 (2010).

[43] G. Khabiri, A. Anokhin, A. Razumnaya, Y. I. Yuzyuk, I. Gueye, B. Carcan, H. Bouyanfif, J. Wolfman, C. Autret-Lambert, and M. El Marssi, Phonon and magnon excitations in Raman spectra of an epitaxial bismuth ferrite film, Phys. Solid State **56**, 2507 (2014).

[44] H. Béa, M. Bibes, S. Petit, J. Kreisel, and A. Barthélémy, Structural distortion and magnetism of $BiFeO_3$ epitaxial thin films: A Raman spectroscopy and neutron diffraction study, Philos. Mag. Lett. **87**, 165 (2007).

[45] X. Li, K. Maute, M. L. Dunn, and R. Yang, Strain effects on the thermal conductivity of nanostructures, Phys. Rev. B **81**, 245318 (2010).

[46] S. Kumar, D. Garcia, J. Jin, and A. Haque, Mechanical strain mediated carrier scattering and its role in charge and thermal transport in freestanding nanocrystalline aluminum thin films, J. Vac. Sci. Technol. B **33**, 022002 (2015).